Ni9Sn2S2: An n-type metal-rich 2D sulfide with a metal-to-metal transition

A. Maignan, S. Hébert, C. Folton, E. Hug, Denis Pelloquin

$Ni_9Sn_2S_2$: An n-type metal-rich 2D sulfide with a metal-to-metal transition

A. Maignan*, S. Hébert, C. Folton, E. Hug and D. Pelloquin

Laboratoire CRISMAT, UMR 6508 CNRS/ENSICAEN/UNICAEN/Normandie Université, 6 bd du Maréchal Juin - F-14050 CAEN Cedex 4 - France.

ABSTRACT

Using spark plasma sintering, a ceramic sample of $Ni_9Sn_2S_2$ sulfide was densified by starting from a powder synthesized in an evacuated ampoule. The powder x-ray diffraction refinements confirm the formation of the *I4/mmm* tetragonal $Ni_9Sn_2S_2$ phase [$a=b$ = 3.6809(2) Å and c = 25.5410(7) Å]. Transmission electron microscopy—imaging and coupled EDX—also reveals the formation of a secondary Ni_6SnS_2 phase and intergrowth defects in the layer stacking between the $Ni_9Sn_2S_2$ and Ni_6SnS_2 phases. More importantly, the structural study demonstrates that $Ni_9Sn_2S_2$ can be described as the n = 2 term of the generic series of compounds, namely, $[Ni_3S_2][Ni_3Sn]_n$. The Ni_3Sn block is of the Cu_3Au cubic form. The measurements of the physical properties show metallic behavior, with ρ_{300K} = 0.135 mΩ cm, a residual resistivity ratio RRR = 2.2, and a Seebeck coefficient S_{300K} = −23.5 μV K^{-1}, indicating an n-type feature, the absolute value of which increases with T, as expected for a metal, to reach S_{650K} = −30 μV K^{-1}. This compound also exhibits a large thermal conductivity, κ_{300K} = 8.0 W K^{-1} m^{-1}, dominated by the electronic part. Interestingly, the small magnetic susceptibility with Pauli-like values shows two transitions at 200 and 125 K, with the first one coinciding to the metal-to-metal transition and to the change of slope in the S(T) curve, suggesting the occurrence of a charge density wave below 200 K. This is discussed in light of the recent developments in topological metals like Ni_3In.

I. INTRODUCTION

The recent growth of the search for quantum materials combined with the need for energy materials opens the field of topological thermoelectric materials.[1] The example given by a Weyl ferromagnet, a $Co_3Sn_2S_2$ shandite,[2] an n-type semi-metal with a large anomalous Nernst effect, in which cobalt lies in kagome layers, shows that metal-rich sulfides are worth studying. A Ni equivalent shandite, $Ni_3Sn_2S_2$, is also to be noticed, as its nonmagnetic Ni^0 ground state[3–5] is marked in contrast to the Co magnetic moment in $Co_3Sn_2S_2$ with Ni Sn_2S_2 showing a lower resistivity and ρ_{300K} = 0.04 mΩ cm,[3] against ρ_{300K} = 0.4 mΩ cm for the $Co_3Sn_2S_2$ shandite n-type metal.[2] Interestingly, with S_{300K} = −20 μV K^{-1}, $Ni_3Sn_2S_2$ belongs to n-type sulfides, a class of thermoelectric chalcogenides in limited number as compared to their p-type counterparts.[6] One interesting peculiarity of $Ni_3Sn_2S_2$ lies in its 5:2 high cation/anion ratio, implying the hetero-metallic bonding between Ni and Sn, and a 2D structural feature along the stacking direction resulting from the covalent bonding between Ni–Sn layers and capping S atoms.

Looking for other metal-rich Ni–Sn–S ternary compounds, it turns out that only $Ni_9Sn_2S_2$ with Ni_6SnS_2 was discovered, and their electronic and crystallographic structures are reported in the pioneering work of Baranov *et al.*[7] who investigated the Ni–Sn–S ternary diagram. In the latter, both compounds were found along the Ni_3Sn–Ni_3S_2 line, with $Ni_9Sn_2S_2$ and Ni_6SnS_2 corresponding to 2:1 and 1:1 ratios of Ni_3Sn and Ni_3S_2. The corresponding atomic structures established from x-ray diffraction on submillimeter size single crystals (0.1 × 0.1 × 0.01 mm^3), extracted from the same batch, led to the intergrowth structures built from two specific slabs $[Ni_3S_2]$ and $[Ni_3Sn]$, respectively,[7] as illustrated by the structural projection of $Ni_9Sn_2S_2$ shown in Fig. 1. These studies have underlined a strong disorder at the level of the $[Ni_3S_2]$ block with the detection of two Ni sites being only partially filled (≈25%) in the case of the $Ni_9Sn_2S_2$ compound. Three specific coordinations were found: square face shared $SnNi_{12}$ cuboctahedron in $[Ni_3Sn]$ blocks and face shared NiS_4 tetrahedra/face shared NiS_5 pyramids in $[Ni_3S_{12}]$ blocks. This structural configuration led to unrealistic

short Ni–Ni bonds as mentioned in Ref. 7. The two ideal structures shown in Fig. 1 were proposed[7] to model the [Ni_3S_2] slabs, either the defective Cu_2Sb type [face shared NiS_5 Fig. 1(a)] or the defective Li_2O type [face shared NiS_4 Fig. 1(b)]. The actual structure would be a random 50–50 distribution of both configurations.

To overcome the limitations coming from the crystal size, we have undertaken the synthesis and characterization of a large dimension polycrystalline and dense $Ni_9Sn_2S_2$ sample to measure the magnetic and thermoelectric properties. On the one hand, the powder x-ray diffraction data and scanning electron microscopy confirm the difficulty of getting rid of the Ni_6SnS_2 minority phase at the microstructural level. For the majority $Ni_9Sn_2S_2$ phase, atomic site occupations refined by the Rietveld method point toward a large Ni deficiency at the level of sulfur-rich layers, in agreement with the initial single crystal report,[7] suggesting a significant amount of atomic disordering at the level of the Ni_3S_2 slabs. On the other hand, the magnetic measurements of the $Ni_9Sn_2S_2$ sample reveal magnetic susceptibility values typical of Pauli-like paramagnetism, but with a T dependence showing two transitions with, for the one at T ≈ 200 K, a corresponding change of slope in both the T-dependent Seebeck coefficient and electrical resistivity curves. The intrinsic nature of this transition is supported by its absence in Ni_3S_2[8,9] and Ni$_3$Sn.[10] Nonetheless, the latter crystallizing in the hexagonal form where Ni forms a kagome network makes the physical properties of $Ni_9Sn_2S_2$ with its cubic Ni_3Sn sublattice worth measuring in the broader context of kagome metals, magnets, and thermoelectrics.[11–14]

II. EXPERIMENTAL

In the first step, a $Ni_9Sn_2S_2$ polycrystalline precursor was synthesized by weighing and mixing in an agate mortar the Ni, Sn, and S elements in a 9:2:2 ratio. A closed ampoule containing this powder was heated at 973 K for 12 h after pumping under primary vacuum and sealing. The re-ground powder was inserted into the graphite die for SPS sintering in an FCT System GmbH. After the application of a uniaxial pressure of 5 kN, the temperature was increased up to 923 K in 14 min by passing dc electric current through the die and then let a plateau at that temperature for 30 min. The temperature was decreased rapidly by stopping the current, allowing it to reach 373 K in only 10 min. A densified pellet (≈99%) of 10 mm diameter was obtained, from which pieces were cut using a diamond wire saw.

A part of the pellet was ground to obtain the powder for x-ray diffraction (XRD) recorded at room temperature with a Panalytical XpertPro diffractometer working with a copper anticathode ($\lambda_{K\alpha1}/_{K\alpha2}$ = 1.5418 Å) and equipped with an X'celerator detector. The data were collected for 1 h in the angular range from 5° to 120° (2θ) with a step of 0.0167°. The X'Pert HighScore Plus Suite working with the PDF2 data bank for phase identification and Fullprof software implemented in the WinPlotr suite[15] were used to analyze these data considering the Rietveld refinements. This crystal analysis was completed by electron microscopy, scanning (SEM) and transmission (TEM) (high resolution "HR" atomic imaging and electron diffraction "ED"), to probe the chemical homogeneity and to detect the potential secondary phases. Coupled scanning atomic imaging (STEM mode)–EDX mapping was also recorded. All this work has been performed using a JEOL F200 TEM equipped with an EDX Centurio spectrometer and ADF-annular bright field (ABF) STEM detectors.

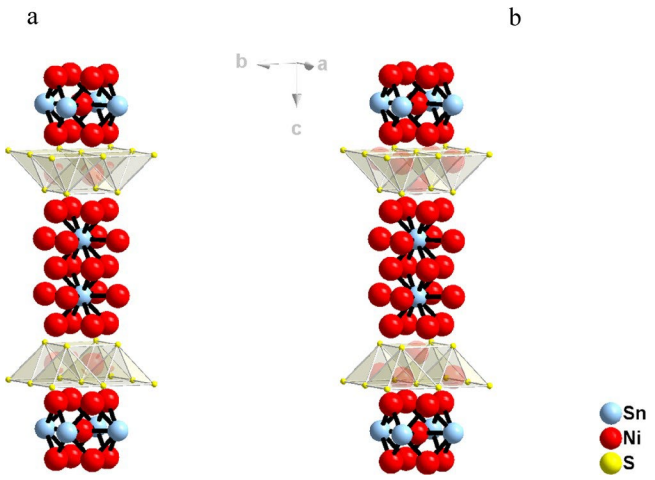

FIG. 1. Schematic structures of $Ni_9Sn_2S_2$ from Ref. 7, considering the stoichiometric Ni_3S_2 slabs of either the Cu_2Sb type (a) or the Li_2O type (b).

A part of the densified material was prepared for metallographic analysis. The simply polished surface (until 1 μm grade) of a piece cut in the densified pellet was observed by optical microscopy, and different constituents of the microstructure were identified by EDS analysis made on a JEOL (JSM-7200F) SEM. In order to have a first insight concerning the mechanical integrity of the structural parts, the Vickers hardness was also measured by a PRESI (MATSUZAWA MMT-X7) micro-hardness tester with 500 gf load.

The magnetic properties were measured using a SQUID magnetometer from Quantum Design. For transport properties below 350 K, a 9T-PPMS (physical properties measurement system from Quantum Design) equipped with either resistivity or thermal transport options was used to measure ρ, S, and κ. For high T measurements (>300 K), a Ulvac Riko ZEM3 system operating under helium partial pressure was used to measure ρ and S; κ was calculated by combining thermal diffusivity and heat capacity data measured with Netzsch systems operating in the N_2 flow.

III. RESULTS

A. Structural characterization

The present powder XRD pattern (Fig. 2) reveals the coexistence of $Ni_9Sn_2S_2$ with Ni_6SnS_2 validated by Rietveld analysis using the *I4/mmm* space group and the reported structural models,[7] allowing the molar fraction to be estimated to ≈80% for the former and ≈12% for the latter. This result is consistent with the results of Ref. 7 for $Ni_9Sn_2S_2$ and Ni_6SnS_2, for which crystals were extracted from a batch obtained from a starting charge of $Ni_9Sn_2S_2$/Ni_6SnS_2/Ni nominal composition. The presence of both phases in crystals and ceramics outlines their proximity on the Ni_3Sn–Ni_3S_2 line of

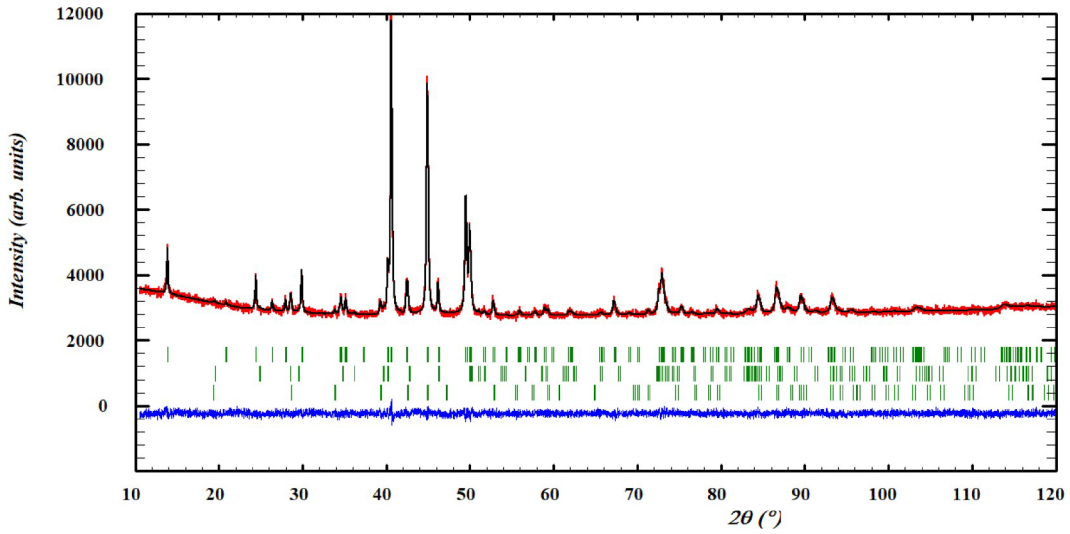

FIG. 2. Experimental (red), calculated (black), and final Rietveld difference (blue) patterns of $Ni_{8.88}Sn_2S_2$. From top to bottom: Green Bragg bars are related to the successive $Ni_{8.88}Sn_2S_2$ (first row) phase and of the secondary $Ni_{5.7}SnS_2$ (middle row) and Ni_3Sn (bottom row) phases.

the Ni–Sn–S ternary phase diagram established at 813 K.[7] As identified from TEM analyses, the remaining small peaks are assigned to the Ni_3Sn phase amounting to about 8% mol. from Rietveld calculations. The unit cell parameters and structural information of the three phases are summarized in Table I, and the final Rietveld difference plot is shown in Fig. 2. The refined values of the unit cell parameters of $Ni_9Sn_2S_2$, $a = b$ = 3.6809(2) Å, c = 25.5410(7) Å, are found to be slightly higher than those reported in Ref. 7 with

TABLE I. Structural parameters of different phases after the final Rietveld refinements. The $Ni_{8.88}Sn_2S_2$, $Ni_{5.7}SnS_2$, and Ni_3Sn formulae and their corresponding mol. fractions can be deduced.

Atom	Wyck.	x	y	Z	B (Å^2)	Occ.	Cell	Phase
Sn1	4e	0	0	0.0742(1)	0.07(4)	1	*I4/mmm*	$Ni_{8.88}Sn_2S_2$
Ni1	4c	0	1/2	0	0.07(4)	1	3.6809(1) Å	
Ni2	8g	0	1/2	0.1489(1)	0.07(4)	1	3.6809(1) Å	
Ni3	4e	1/2	1/2	0.0716(2)	0.07(4)	1	25.5410(7) Å	R_{Bragg} 4.36
S1	4e	1/2	1/2	0.2017(3)	0.07(4)	1	90.0°	
Ni4	4e	1/2	1/2	0.2776(8)	0.07(4)	0.267(1)	90.0°	Fract (%):
Ni5	4d	0	1/2	1/4	0.07(4)	0.174(7)	90.0	80.7(7)
Sn1	2a	0	0	0	0.1(2)	1	*I4/mmm*	$Ni_{5.7}SnS_2$
Ni1	8g	0	1/2	0.1061(8)	0.1(2)	1	3.6496(2) Å 3.6496(2) Å	
Ni2	2b	1/2	1/2	0	0.1(2)	1	18.1606(25) Å	
S	4e	1/2	1/2	0.180(2)	0.1(2)	1	90.0°	R_{Bragg} 8.15
Ni3	4e	0	0	0.204(5)	0.1(2)	0.24(4)	90.0°	Fract (%):
Ni4	4d	0	1/2	1/4	0.1(2)	0.11(4)	90.0°	11.7(4)
Sn	2c	1/3	2/3	1/4	0.1[a]	1	*P6$_3$/mmc*	Ni_6Sn_2
Ni	12j	0.8366	0.678 53	0.250 00	0.1[a]	0.5	5.2919(3) Å	
							5.2919(3) Å	R_{Bragg} 9.40
							4.2455(5) Å	
							90.0°	Fract (%):
							90.0°	
							120.0	7.6(2)

[a]Arbitrarily fixed.

$a = b$ = 3.671 Å, c = 25.474 Å, which might indicate a slight difference in compositions. From occupation site refinements, a large deficiency close to 78% at Ni sites surrounding the sulfur atoms is also confirmed at the level of the Ni_xS_2 slabs. These calculations lead to the actual $Ni_{8.88}Sn_2S_2$ composition for the nominal $Ni_9Sn_2S_2$ (Table I).

The presence of these phases was also confirmed by the microstructure study. At a large scale, the optical micrographs show multiphase and overall homogeneous microstructures (Fig. 3). In Fig. 3(a), clusters of purple particles and isolated and largest white plates are easily distinguished, both constituents lying in a less contrasted granular matrix. EDS mapping coupled with the local atomic composition measurements allowed us to associate different parts of the microstructure to the phases of the Ni–Sn–S diagram. The purple particles correspond to Ni_3Sn with some pure Sn residual nodules. In this area, the matrix is associated to the $Ni_9Sn_2S_2$ phase [Fig. 3(b)]. The composition of the white plates [Fig. 3(c)] is consistent with Ni_3S_2, a compound that was not detected by XRD analysis. Although the white plates are often big and well detectable, an image analysis showed that, indeed, they occupy less than 1% of the total observed surface (18 mm^2). In the biggest plates of Ni_3S_2, EDS mappings also point to the presence of Ni- and Sn-rich intermetallic precipitates that have grown in epitaxy with the sulfide [Fig. 3(d)]. The dark shells [Fig. 3(c)], in which the white plates are always embedded, were identified as Ni_6SnS_2. The presence of this phase in the rest of the matrix is more difficult to evidence in agreement with Rietveld analysis that points out a molar fraction close to 12%. To complete the microstructure study, hardness measurements were made, giving an average Vickers hardness value of 3.1 GPa. The areas around indentations are free of long cracks but show deformations that seem to result from a weakness of the grain boundaries or sheets delamination inside the grains [Fig. 3(e)]. Irreversible deformation mechanisms also appear around the hardness imprints. This suggests the possibility of obtaining materials with acceptable toughness, to be used as legs of thermoelectric modules. Finally, at the microstructure scale, the material is well densified, with a particularly low porosity of around 1% on the observed surface consistent with the compacity value measured on densified pellets.

In order to evidence a possible structural relationship at the atomic level between the stacking mode of $Ni_9Sn_2S_2$ and Ni_6SnS_2, a STEM study was conducted. In a large majority of the observed crystallites, electron diffraction (ED) confirms the $Ni_9Sn_2S_2$ structure as the main phase with a periodicity close to 25.5 Å along c (top right inset of Fig. 4). The experimental and corresponding calculated (inset) high-resolution STEM images along the layers' stacking direction (Fig. 4) confirm the description of the $Ni_9Sn_2S_2$ structure as a 1:1 regular stacking of two specific slabs, S1 (Ni_3Sn) and S2 (Ni_3S_2), with a thickness of 7.6 and 5.2 Å, respectively.[7] On this [100] atomic HAADF image, Sn species rows are highlighted and spaced of 3.65 Å along the b direction, whereas these typical contrasts are shifted of 1.85 Å along the same direction of every successive S1 slab, in agreement with the I-type space group. In only about 10% of the analyzed crystallites, the ED pattern yields a c value close to 18 Å corresponding to the Ni_6SnS_2 structure where S1 is only 3.8 Å thick. In these structural models,[7] the $[Ni_{1+2n}Sn_n]_\infty$ heterometallic blocks related to the S1 slab in $Ni_9Sn_2S_2$ (n = 2) or Ni_6SnS_2 (n = 1) alternate with sulfur-rich Ni_xS antifluorite or NaCl-type layers related to the S2 slab. Another description can be proposed by considering a shared Ni_2 slice between the successive S1 and S2 slabs leading to the generic intergrowth formula $[Ni_3S_2]_m[Ni_3Sn]_n$, $Ni_9Sn_2S_2$ corresponding to the (m = 1, n = 2) term. This intergrowth feature might favor the formation of stacking faults. Indeed, such defects are evidenced from STEM imaging, especially in the thickness of the Ni_3Sn slab as illustrated by Fig. 5. These defects highlight the coexistence of the Ni_6SnS_2 (n = 1) member inside the $Ni_9Sn_2S_2$ matrix, which locally changes the chemical composition. Also, EDX mapping at the level of these defects reveals a few Sn-free inclusions of the $Ni_{1.66}S$ composition, as shown in Fig. S1 in the supplementary material, that could be linked to the Ni_3S_2 white plates depicted by optical observations in a larger scale (Fig. 3). In the present study, the EDX quantifications performed on five different crystallites, assuming the expected $Ni_9Sn_2S_2$ stoichiometry, lead to the average $Ni_{8.71}Sn_{2.27}S_{2.02}$ composition. This result reveals some slight Ni and Sn deviations that can be linked to the observed defects in the $Ni_9Sn_2S_2$ matrix, but it remains consistent with the $Ni_{8.88}Sn_2S_2$ chemical composition deduced from Rietveld analysis (Table I). In order to identify the atoms along the stacking direction, coupled atomic STEM imaging–EDX experiments have been carried out. This work has been made in the annular bright field (ABF) mode to highlight the sulfur rows. The atomic ABF image recorded along the [100] zone axis (Fig. S2 in the supplementary material) shows a bright zig zag contrast corresponding to the S rows in the S2 slabs. They are spaced by the darker 7.6 Å thick S1 blocks, showing two rows of black dots corresponding to Sn with its much larger Z number as compared to S and Ni. Interestingly, the simultaneous collection of atomic elemental EDX mapping and ABF image confirms the overall atomic stacking and also that S2 is mainly composed of S with only a few Ni species between the rows of sulfur while S1 contains both Sn and Ni species. From the chemical profiles shown in Fig. S2 in the supplementary material, we conclude that Ni species sit in the S1 slabs and at the interface with the S2 slabs containing sulfur. This leads to the formation of Ni_xS– NaCl-type layers only and the Ni_xS–LiO_2-type layers invoked in Ref. 7 (Fig. 1) being lacking in the TEM images.

B. T-dependent resistivity, Seebeck coefficient, and thermal conductivity

Though a metallic state was predicted by the electronic band structure calculation,[7] no experiments were reported to support this assumption. The electrical resistivity of the SPS-densified material is characteristic of metallic behavior with $d\rho/dT > 0$, independent of the temperature T (Fig. 6, right y axis). The resistivity increases from $\rho_{5K} = 0.065$ mΩ cm up to $\rho_{670K} = 0.165$ mΩ cm with a residual resistivity ratio (RRR) between 5 and 300 K equal to 2.2. In addition, a metal-to-metal transition can be detected at about 200 K, below which the ρ decrease is more pronounced. At 300 K, the value $\rho = 0.135$ mΩ cm lies close to that of polycrystalline Ni_3S_2 sulfide $\rho = 0.1$ mΩ cm[8] but is much higher than the value reported for the hexagonal (kagome) Ni_3Sn polycrystalline alloy with $\rho \approx 0.017$ mΩ cm.[10] As shown in the inset of Fig. 6, the low T resistivity can be described by the Bloch–Grüneisen law, with a Debye

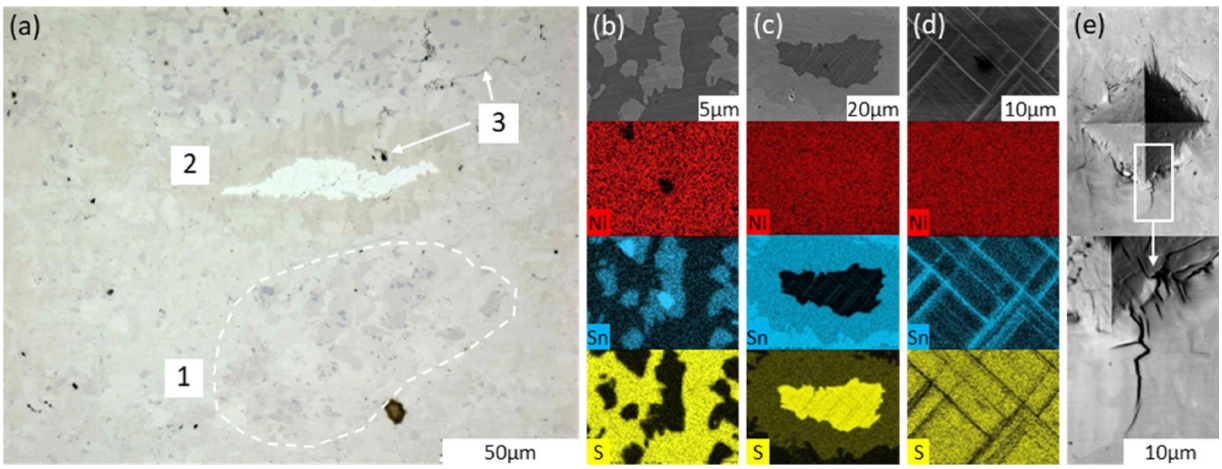

FIG. 3. Microstructure characterization. (a) Optical microscopy; different constituents of the microstructure: 1, a cluster of purple particles; 2, a white plate in its darker shell; 3, in black, isolated porosity and grain decohesion. (b)–(d) SEM images with EDS mappings; (b) Ni_3Sn particles in the $Ni_9Sn_2S_2$ matrix. (c) Ni_3S_2 sulfide plate in its Ni_6SnS_2 shell. (d) Precipitation of a Ni–Sn rich intermetallic in the sulfide, Ni_3S_2. (e) Deformations around a Vickers indentation obtained by confocal microscopy.

temperature θ_D = 215 K [$\rho(T) = \rho(0) + A(T/\theta_D)^5 \times J_5(T/\theta_D)$] suggesting a classical electron–phonon diffusion mechanism. The metallic nature of $Ni_9Sn_2S_2$ is consistent with the linearity of the Seebeck coefficient as T increases up to 670 K (Fig. 6, left y axis), while its negative sign (S < 0) indicates a behavior dominated by n-type carriers. Furthermore, similar to the transition observed at ≈200 K in the ρ(T) curve, a change of slope is also present in S(T) at the same temperature. At T = 300 K, the S = −23.5 µV K^{-1} value is very close to that of $Ni_3Sn_2S_2$ shandite,[3] despite the fact that its metal/sulfur ratio differs. Finally, the superimposition of the cooling curve to the heating one between 300 and 670 K indicates that the sample is chemically stable at least up to 670 K, i.e., the highest T used for S and ρ measurements.

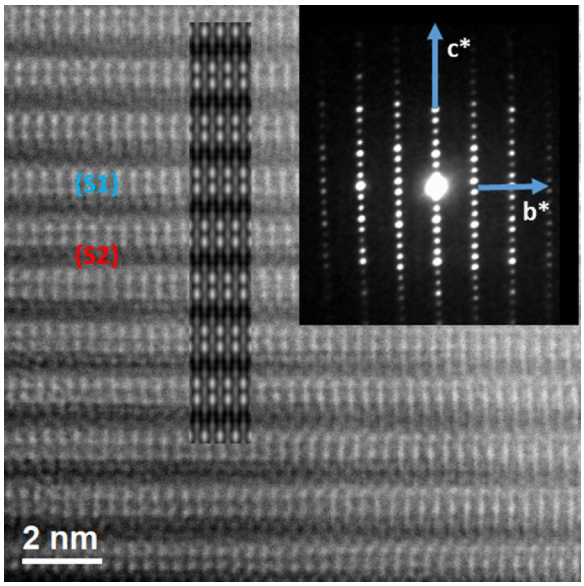

FIG. 4. Experimental ED [100] pattern and the corresponding HAADF image of $Ni_9Sn_2S_2$. The calculated ADF image is superimposed on the experimental image. The S1 and S2 labels are related to the Ni_3Sn and Ni_3S_2 slabs, respectively.

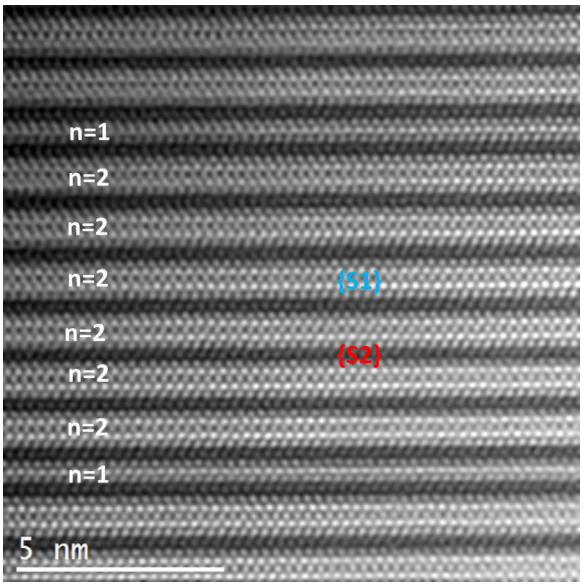

FIG. 5. Experimental [110] HAADF images with defects of n = 1 member in the main n = 2 matrix.

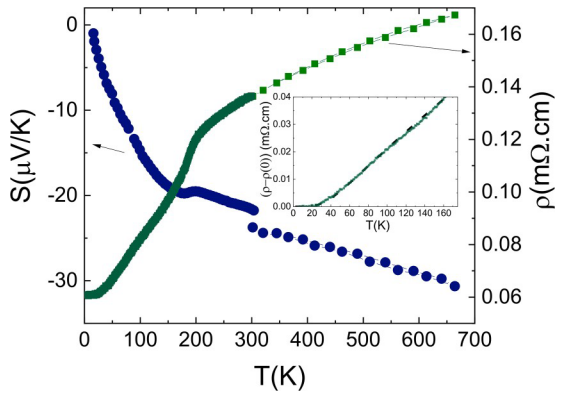

FIG. 6. T dependence of electrical resistivity ρ (right y axis) and Seebeck coefficient S (left y axis). The inset represents the Bloch–Grüneisen fitting (dash black line), with $\rho(T) - \rho(0) = A(T/\theta_D)^5 J_5(T/\theta_D)$, with $\theta_D = 215$ K.

In terms of thermoelectricity, such values allow a maximum value for the power factor ($PF = S^2/\rho$) to be reached at the highest T (=670 K), PF = 0.55 mW m^{-1} K^{-2}, a value comparable to those of metal sulfides.[6] For instance, $Cu_{11}MnSb_4S_{13}$ tetrahedrite with a TE figure merit $zT > 1$ [$zT = T*(PF/\kappa)$] exhibits at 575 K PF = 0.52 mW m^{-1} K^{-2} but with a combination of a much higher resistivity and Seebeck values.[16] This $Ni_9Sn_2S_2$ PF value is smaller by one order of magnitude than that of alloys containing similar elements like Ni_3Sn, with PF = 4 mW m^{-1} K^{-2} at 670 K.[10] The zT values of $Ni_9Sn_2S_2$ are modest as a result of the too large thermal conductivity, κ, reaching at 650 K κ = 11.1 W m^{-1} K^{-1} (Fig. S3 in the supplementary material), especially when compared to the ultra-low value of some sulfides, like $\kappa_{(575K)} = 0.26$ W m^{-1} K^{-1} for $Cu_{11}MnSb_4S_{13}$, thus yielding a zT value 40 times larger, despite a similar PF. On the opposite, the very large κ of Ni_3Sn,

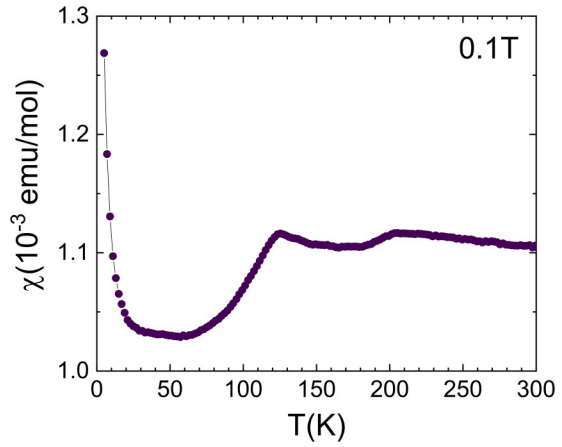

FIG. 7. T dependence of the magnetic susceptibility (χ). The data correspond to the zero-field-cooling measurements in 0.1 T.

$\kappa_{(670K)} = 40$W m^{-1} K^{-1}, eventually makes its zT (=0.07 at 670 K[10]) of the same order as that of $Ni_9Sn_2S_2$ with zT = 0.03 at the same T. This suggests that for $Ni_9Sn_2S_2$, chemical substitutions and/or nano-engineering should be performed in order to reduce its thermal conductivity and optimize the electronic band structure.

C. Magnetic susceptibility, magnetization hysteresis loops, and magnetoresistance

The T-dependent magnetic susceptibility χ(T) (Fig. 7) collected in a zero-field-cooling mode (zfc) in 0.1 T shows very low χ (=M/H) magnetic susceptibility values in the range of 1.05×10^{-3} -1.5×10^{-3} emu/mol for the T range of the measurements. Such low values are typical of Pauli-like paramagnetism, a magnetic behavior evidenced for Ni_3S_2 and $Ni_3Sn_2S_2$ shandites.[3,8] As no transition could be detected in the same T region on the χ(T) curves reported for Ni_3S_2 and $Ni_3Sn_2S_2$,[3,8] the present result appears to be the intrinsic behavior of $Ni_9Sn_2S_2$. Taking into account the diamagnetic contribution of the elements (Ni, Sn, and S), the mean values of χ are closer to 1.3×10^{-3} emu/mol rather than 1.1×10^{-3} emu/mol. For comparison, the χ values are 1.5×10^{-4} emu/mol for Ni_3S_2,[8] suggesting a much larger density of states $D(E_F)$, by a factor close to 7 for $Ni_9Sn_2S_2$. Moreover, the χ(T) curve exhibits two transitions: at T ≈ 200 K and T ≈ 125 K. This transition temperature close to 200 K corresponds to the changes of slopes detected in ρ(T) and S(T) measurements (Fig. 6). These χ decreases, together with a metal-to-metal transition at 200 K, are reminiscent of a charge density wave transition. The decrease observed at 125 K would correspond to about 7% of the susceptibility, suggesting a loss of 7% of the carriers in a simple model. Note that, however, the susceptibility transition is more important at 125 than at 200 K, and that the one at 125 K has no clear impact on the transport. If the two transitions observed on χ are really linked to a structural instability such as CDW, it would thus suggest a subtle interplay with the carriers. The resistivity curves have been measured with different currents (from 10 to 100 mA) and do not depend on the current values, but a more specific investigation of the non-linear transport properties is necessary to probe a possible CDW like in other Ni sulfides, such as in KNi_2S_2.[17]

IV. DISCUSSION AND CONCLUDING REMARKS

These first TEM results at the atomic scale for $Ni_9Sn_2S_2$ have confirmed the expected stacking mode that can be written as an intergrowth of the generic $[Ni\ S_3]^{S2}_2[Ni\ Sn]^{S1}_n$ formula. The presence of structural defects may explain that the local composition from EDX-TEM, $Ni_{8.71}Sn_{2.27}S_{2.02}$, slightly differs from the refined formula obtained with the XRD data, $Ni_{8.88}Sn_2S_2$, both showing a Ni deficiency as compared to the "Ni_9" nominal content, similarly to isostructural germanates.[18] As shown by the calculated images that fit well with our experimental ABF-ADF images, these TEM observations (Fig. S2 in the supplementary material) allow us to choose a single structural NaCl-type NiS_2 layer rather than a Ni_xS–LiO_2-type layer[7] to describe the sulfur-rich slabs [Fig. 1(a) and 1(b)]. Similar conclusions were drawn for the analogous $Ni_{7-\delta}SnQ_2$ (Q = Se and Te) series related to the n = 1 member.[19,20] These structural studies of compounds with formula close to that of Ni_6SnS_2 showed a structural modulation linked to an ordered variation of the Ni sites

occupancy in the S2 slabs. The significant increase in the thickness of chalcogenide-based slabs with the sulfur content x in $Ni_{7-\delta}InSe_{2-x}S_x$ ($1.26 \geq \delta \geq 0.94$; $0 \leq x \leq 1.33$) was found to go with the increase in the Ni content,[20] giving a chemical origin to the modulated feature. Similarly, a structural modulation might be at play in $Ni_9Sn_2S_2$ in connection with the Ni deficiency in the $[Ni_{3-\epsilon}S_2]$ slabs. Also, the presence of intergrowth between the n = 1 and n = 2 terms observed by STEM atomic imaging points toward a possibility of generating new compounds, if regular intergrowths could be scaled up.

At T = 200 K, $Ni_9Sn_2S_2$ exhibits a metal-to-metal transition associated to a change of slope in the S(T) curve and a concomitant decrease in magnetic susceptibility, a phenomenon not reported in Ni_3Sn nor Ni_3S_2. The possible existence of a charge density wave setting below that T would deserve additional measurements. In that respect, the growth of large enough crystals is needed.

Interestingly, the quadratic symmetry of 2D $Ni_9Sn_2S_2$ sulfide related to the cubic Cu_3Au-type structure of its heterometallic $[Ni_3Sn]_2^{S1}$ block makes that metal-rich sulfide different from the kagome metal, like hexagonal Ni_3In, and its promising thermoelectric properties coming from the topological flatband feature.[10–14] Still, the $Ni_9Sn_2S_2$ Seebeck coefficient sign and value at room T are very similar to those reported for hexagonal Ni_3In and Ni_3Sn polycrystalline samples with flatbands,[10] $S_{300K} = -23.5\ \mu V\ K^{-1}$ for $Ni_9Sn_2S_2$ against $S_{300K} \approx -20\ \mu V\ K^{-1}$ for Ni_3In and Ni_3Sn. Also note that in $Ni_9Sn_2S_2$, very similar properties are measured as in topological materials such as ScV_6Sn_6,[13] which exhibits a metal-to-metal transition at 100 K and a decrease of the magnetic susceptibility due to the formation of a charge density wave or in AV_5Sb_3 kagome metals.[21,22] In that respect, the existence of two transitions in the χ(T) of $Ni_9Sn_2S_2$ would be consistent with the observation of successive charge density waves or successive electronic and lattice instabilities, as recently discussed in compounds such as kagome superconductors.[22,23]

Nonetheless, as flatbands are not expected from the density of state calculations in $Ni_9Sn_2S_2$,[7] the electronic properties are, in our case, more likely governed by electron–phonon interactions. Compared to these topological materials, even if a similar Seebeck coefficient is obtained as the one of Ni_3Sn, the main difference lies in the higher $Ni_9Sn_2S_2$ resistivity, hence yielding a lower power factor. This might reflect the 2D structural feature resulting from the presence of S layers with covalent Ni–S bonding. The anisotropy of the properties in connection to that of the electronic structure would deserve further calculations and measurements to elucidate if the DOS at the Fermi level explains the smaller power factor and if an optimum doping could be achieved.

SUPPLEMENTARY MATERIAL

Some experimental [110] HAADF images with defects in $Ni_9Sn_2S_2$ (Fig. S1) reveal Sn-free inclusion in the main matrix as shown by the corresponding elemental EDX mapping collected in the red window. It confirms the presence of only Ni and S in these defective regions.

The ABF [100] image and the corresponding over mapping of Ni–S and Sn–S species (left and right parts of Fig. S2, respectively) confirm these chemical elements' separation in the atomic layers along the c axis, where the S-rich layers alternate with heterometallic mixed Ni/Sn layers, as expected from the structural model. In the experimental image (central part of Fig. S2), the elemental EDX intensity profiles extracted along the stacking direction c support that separation with S-free and S-rich alternating layers. The good fitting of the calculated ABF image from the proposed structural model to the experimental image is demonstrated.

In Fig. S3, the thermal conductivity κ as a function of temperature (black dots) increases with T. This trend reflects the increase with T of the electronic part (κ_{elec}) calculated from the Wiedemann–Franz Law as also shown in the figure (blue dots).

AUTHOR DECLARATIONS

Conflict of Interest

The authors have no conflicts to disclose.

Author Contributions

A. Maignan: Conceptualization (lead); Supervision (equal); Writing – original draft (lead); Writing – review & editing (equal). S. Hébert: Data curation (equal); Formal analysis (equal); Investigation (equal); Supervision (equal); Validation (equal); Writing – original draft (equal); Writing – review & editing (equal). C. Folton: Data curation (equal); Formal analysis (equal); Investigation (equal); Writing – original draft (equal); Writing – review & editing (equal). E. Hug: Investigation (equal); Validation (equal); Writing – original draft (equal); Writing – review & editing (equal). D. Pelloquin: Data curation (equal); Formal analysis (equal); Investigation (equal); Validation (equal); Writing – original draft (equal); Writing – review & editing (equal).

DATA AVAILABILITY

The data that support the findings of this study are available from the corresponding author upon reasonable request.

REFERENCES

[1]C. Fu, Y. Sun, and C. Felser, "Topological thermoelectrics," APL Mater. 8, 040913 (2020).

[2]S. N. Guin, P. Vir, Y. Zhang, N. Kumar, S. J. Watzman, C. Fu, E. Liu, K. Manna, W. Schnelle, J. Gooth, C. Shekhar, Y. Sun, and C. Felser, "Zero-field Nernst effect in a ferromagnetic Kagome-lattice Weyl-semimetal $Co_3Sn_2S_2$," Adv. Mater. 31, 1806622 (2019).

[3]A. Aziz, P. Mangelis, P. Vaqueiro, A. V. Powell, and R. Grau-Crespo, "Electron and phonon transport in shandite-structured $Ni_3Sn_2S_2$," Phys. Rev. B 94, 165131 (2016).

[4]P. Gütlich, K.-J. Range, C. Felser, C. Schultz-Münzenberg, W. Tremel, D. Walcher, and M. Waldeck, "The valence states of nickel, tin, and sulfur in the ternary chalcogenide $Ni_3Sn_2S_2$: XPS, ^{61}Ni and ^{119}Sn Mössbauer investigations, and band structure calculations," Angew. Chem. Int. Ed. 38, 2381 (1999).

[5]T. Kubodera, H. Okabe, Y. Kamihara, and M. Matoba, "Ni substitution effect on magnetic and transport properties in metallic ferromagnet $Co_3Sn_2S_2$," Physica B 378–380, 1142 (2006).

[6]F.-H. Sun, H. Li, J. Tan, L. Zhao, X. Wang, H. Hu, C. Wang, and T. Mori, "Review of current ZT > 1 thermoelectric sulfides," J. Materiomics 10, 218 (2024).

[7]A. I. Baranov, A. A. Isaeva, L. Kloo, and B. A. Popovkin, "New metal-rich sulfides Ni_6SnS_2 and $Ni_9Sn_2S_2$ with a 2D metal framework: Synthesis, crystal structure, and bonding," Inorg. Chem. 42, 6667–6672 (2003).

[8]P. A. Metcalf, B. C. Crooker, M. McElfresh, Z. Kykol, and J. M. Honig, "Low-temperature electronic anti magnetic properties of single-crystal Ni_3S_2," Phys. Rev. B 50, 2055 (1994).
[9]Z. W. Lu, B. M. Klein, and D. J. Singh, "Electronic structure of heazlewoodite Ni_3S_2," Phys. Rev. B 54, 13542 (1996).
[10]F. Garmroudi, I. Serhiienko, S. Di Cataldo, M. Parzer, A. Riss, M. Grasser, S. Stockinger, S. Khmelevskyi, K. Pryga, B. Wiendlocha, K. Held, T. Mori, E. Bauer, and A. Pustogow, "High thermoelectric power factor through topological flat bands," arXiv:2404.08067v1 [cond-mat.str-el] (2024).
[11]L. Ye, S. Fang, M. G. Kang, J. Kaufmann, Y. Lee, J. Denlinger, C. Jozwiak, A. Bostwick, E. Rotenberg, E. Kaxiras, D. C. Bell, O. Janson, R. Comin, and J. G. Checkelsky, "A flat band-induced correlated kagome metal," Nat. Phys. 20, 610–614 (2024).
[12]J. X. Yin, B. Lian, and M. Z. Hasan, "Topological kagome magnets and superconductors," Nature 612, 647–657 (2022).
[13]H. W. Suriya Arachchige, W. R. Meier, M. Marshall, T. Matsuoka, R. Xue, M. A. McGuire, R. P. Hermann, H. Cao, and D. Mandrus, "Charge density wave in Kagome lattice intermetallic ScV_6Sn_6," Phys. Rev. Lett. 129, 216402 (2022).
[14]J. G. Checkelsky, B. A. Bernevig, P. Coleman, S. Qimiao, and S. Paschen, "Flat bands, strange metals and the Kondo effect," Nat. Rev. Mater. 9, 509–526 (2024).
[15]T. Roisnel and J. Rodríquez-Carvajal, "WinPLOTR: A windows tool for powder diffraction pattern analysis," Mater. Sci. Forum 378–381, 118–123 (2001).
[16]J. Heo, G. Laurita, S. Muir, M. A. Subramanian, and D. A. Keszler, "Enhanced thermoelectric performance of synthetic tetrahedrites," Chem. Mater. 26, 2047–2051 (2014).
[17]J. R. Neilson, T. M. McQueen, A. Llobet, J. Wen, and M. R. Suchomel, "Charge density wave fluctuations, heavy electrons, and superconductivity in KNi_2S_2," Phys. Rev. B 87, 045124 (2013).
[18]A. A. Isaeva, A. I. Baranov, L. Kloo, M. Ruck, and B. A. Popovkin, "New metal-rich mixed chalcogenides with intergrowth structures: $Ni_{8.21}Ge_2S_2$ and $Ni_{8.45}Ge_2Se_2$," Solid State Sci. 11, 1071–1076 (2009).
[19]A. I. Baranov, A. A. Isaeva, L. Kloo, R. A. Kulbachinskii, R. A. Lunin, V. N. Nikiforov, and B. A. Popovkin, "2D metal slabs in new nickel-tin chalcogenide $Ni_{(7-\delta)}SnQ_2$ (Q = Se Te): Crystal and electronic structure, chemical bonding and physical properties," J. Solid State Chem. 177, 3616–3625 (2004).
[20]A. Dutta, K. Buxi, A. Lakshan, A. Mondal, F. Wang, and P. P. Jana, "Role of partial vacancy and structural distortion in the stability of nonstoichiometric phases $Ni_{7-\delta}InSe_{2-x}S_x$ ($1.26 \geq \delta \geq 0.94$; $0 \leq x \leq 1.33$)," Inorg. Chem. 62, 17894–17904 (2023).
[21]B. R. Ortiz, L. C. Gomes, J. R. Morey, M. Winiarski, M. Bordelon, J. S. Mangum, I. W. H. Oswald, J. A. Rodriguez-Rivera, J. R. Neilson, S. D. Wilson, E. Ertekin, T. M. McQueen, and E. S. Toberer, "New Kagome prototype materials: Discovery of KV_3Sb_5, RbV_3Sb_5, and CsV_3Sb_5," Phys. Rev. Mater. 3, 094407 (2019).
[22]S. D. Wilson and B. R. Ortiz, "AV_3Sb_5 Kagome superconductors," Nat. Rev. Mater. 9, 420 (2024).
[23]A. Subedi, "Order-by-disorder charge density wave condensation at q = (1/3,1/3,1/3) in Kagome metal ScV_6Sn_6," Phys. Rev. Mater. 8, 014006 (2024).